



RESEARCH ARTICLE

Diagnosing the fast-heating process of the double-cone ignition scheme with X-ray spectroscopy

Yu Dai^{1,2}, Haochen Gu^{1,2}, Ke Fang¹, Yihang Zhang¹, Chenglong Zhang^{1,3}, Yufeng Dong¹, Zhe Zhang^{1,4,5}, Xiaohui Yuan^{4,6}, Yutong Li^{1,2,4,5}, and Jie Zhang^{1,4,6}

¹Beijing National Laboratory for Condensed Matter Physics, Institute of Physics, Chinese Academy of Sciences, Beijing, China

²School of Physical Sciences, University of Chinese Academy of Sciences, Beijing, China

³State Key Laboratory for Tunnel Engineering, China University of Mining and Technology, Beijing, China

⁴Collaborative Innovation Center of IFSA, Shanghai Jiao Tong University, Shanghai, China

⁵Songshan Lake Materials Laboratory, Dongguan, China

⁶Key Laboratory for Laser Plasma (MOE) and School of Physics and Astronomy, Shanghai Jiao Tong University, Shanghai, China

(Received 7 April 2024; revised 16 May 2024; accepted 24 May 2024)

Abstract

In the double-cone ignition scheme of inertial confinement fusion, the head-on collision of two compressed fuel jets from the cone-tips forms an isochoric plasma, which is then heated suddenly by a MeV relativistic electron beam produced by ultra-intense picosecond laser pulses. This fast-heating process was studied experimentally at the Shenguang II upgrade laser facility. By observing temporal-resolved X-ray emission and the spatial-resolved X-ray spectrum, the colliding process and heating process are carefully studied. The colliding plasma was imaged to have dimensions of approximately 86 μm in the implosion direction and approximately 120 μm in the heating direction. By comparing the simulated plasma X-ray spectrum with experimental data, the electron temperature of the heated plasma was found to rapidly increase to 600 ± 50 eV, almost doubling the temperature achieved before the heating laser incidence.

Keywords: direct drive; fast ignition; inertial confinement fusion; plasma spectroscopy

1. Introduction

The scientific feasibility of inertial confinement fusion was demonstrated by the first success of deuterium-tritium (DT) fusion ignition at the National Ignition Facility (NIF) in December 2022^[1,2]. However, the coupled compression and heating processes in the central ignition scheme lead to instabilities of compression and low heating efficiency. Fast ignition was proposed as an alternative approach for high-gain laser fusion because it decouples fuel compression from fuel ignition, leading to a more stable compression and efficient ignition^[3].

In the fast ignition scheme, ultra-intense laser pulses are utilized to generate a relativistic electron beam (REB),

injecting into the pre-compressed isochoric plasma. The REB then travels forward as a strong current, heating the high-density fuel to generate a hot spot^[4–8]. Research conducted over the past few decades has demonstrated that a guiding cone for heating could enhance efficiency by reducing the distance from the source to the core. This method has shown promising results in experiments and holds potential for further advancements in the field of fast ignition^[8–12]. However, generating isochoric high-density plasmas with sharp ends has been challenging.

One emerging solution comes with the double-cone ignition (DCI) scheme^[13]. The DCI scheme employs focused nanosecond laser beams to implode the DT fuels embedded in two head-on gold cones; the collision of compressed plasma jets from the tips of the cones forms an isochoric plasma with sharp ends so that the high-current REB in 10 ps, guided by a kilo-tesla magnetic field^[14], may be efficiently injected into the compressed fuel to trigger ignition suddenly. Positioned between the main cones is a heating cone, with its closed end directed towards the collision

Correspondence to: Z. Zhang, Beijing National Laboratory for Condensed Matter Physics, Institute of Physics, Chinese Academy of Sciences, Beijing 100190, China. Email: zzhang@iphy.ac.cn; J. Zhang, Key Laboratory for Laser Plasma (MOE) and School of Physics and Astronomy, Shanghai Jiao Tong University, Shanghai 200240, China. Email: jzhang1@sjtu.edu.cn

point at a distance of tens of micrometers. An ultra-intense laser pulse is then directed into the heating cone to generate energetic electrons that heat the fuel. Previous experiments have successfully validated the first three steps of the DCI scheme^[15]. Eight compressing laser beams with a total energy of 14 kJ were used to drive chlorine-doped polystyrene shells ($C_{16}H_{14}Cl_2$, $CHCl$), resulting in a colliding plasma with a central density of up to a few g/cm^3 , an areal density of 100 mg/cm^2 and a confinement time of 200 ps. The head-on collision effectively enhances the density of the plasma by several times, preheats the fuel and efficiently converts kinetic energy into internal energy.

The DCI scheme allows for a relatively low implosion velocity, resulting in only 20%–30% of the internal energy of the fuel being obtained from the compressing lasers, with the remaining 70%–80% required being obtained from the heating lasers^[10]. Therefore, fast heating plays a crucial role in the DCI scheme. In this study, we have conducted an experiment to investigate the fast-heating effect in DCI at the Shenguang II upgrade laser facility (SG-II UP). Through the analysis of time-resolved X-ray images and spatially resolved spectra, it is confirmed that the high-density collisional plasma is significantly heated by the heating laser beam. The observation of 2.7–2.8 keV Cl K-emission lines from the collisional plasma allows for temperature estimation by comparing the calculated emission spectrum using a collisional-radiative code. The analysis reveals that the implosion core is heated to $600 \pm 50\text{ eV}$, nearly twice the temperature achieved before fast heating.

2. Experimental details

The experiment was performed at the SG-II UP, Shanghai Institute of Optics and Fine Mechanics, Chinese Academy of Sciences. As shown in Figure 1(a), eight compressing laser

beams at $0.351\text{ }\mu\text{m}$ and one heating laser beam at $1.05\text{ }\mu\text{m}$ were employed to compress and heat the fuel, respectively. The total energy of the compressing lasers was 14 kJ with 4.7 ns duration. For uniform irradiation, continuous phase plates (CPPs) were used to smooth the compressing beams resulting in a $\phi = 700\text{ }\mu\text{m}$ focusing spot for every single beam. The waveform of the compressing lasers shown in Figure 1(b) was designed by Multi-1D code^[16], and has been optimized with an artificial intelligence algorithm to achieve a quasi-isentropic compression^[17]. Simulated results from Multi-1D accorded quite well with the experimental results on the shell velocity of the plasma jets ejected from the vertex. Two spherical shells placed in the main cones were compressed and accelerated towards the geometric center by direct driving and finally collided together at the center of the two cones. The material of the shells was chlorine-doped polystyrene in which Cl is at 6% atomic fraction. When the areal density of the colliding plasma came to the maximum, the heating laser beam of 500 J with 10 ps duration was injected on a golden planar target assembled between the two cones to produce fast electrons. The incident angle is 9° from the normal of the golden plane. The heating cone was replaced by a golden plane here to reduce the difficulty in assembling and aiming. The focal spot of the heating laser was $30\text{ }\mu\text{m}$ in diameter, which leads to $I\lambda^2 = 7.7 \times 10^{18}\text{ W}\cdot\mu\text{m}^2\cdot\text{cm}^{-2}$. The thickness of the golden plane was $20\text{ }\mu\text{m}$ and its rear surface was $46\text{ }\mu\text{m}$ from the colliding center.

As for diagnosis, an X-ray Kirkpatrick–Baez (KB) microscope coupled with a framing camera was installed on the equator nearly perpendicular to the heating laser to monitor the time-resolved self-emission of the colliding plasma. Its spatial and temporal resolutions were approximately $10\text{ }\mu\text{m}$ and 90 ps, respectively. The camera was made responsive to X-rays from 1.0 to 3.5 keV by installing a $25\text{ }\mu\text{m}$ beryllium filter^[18].

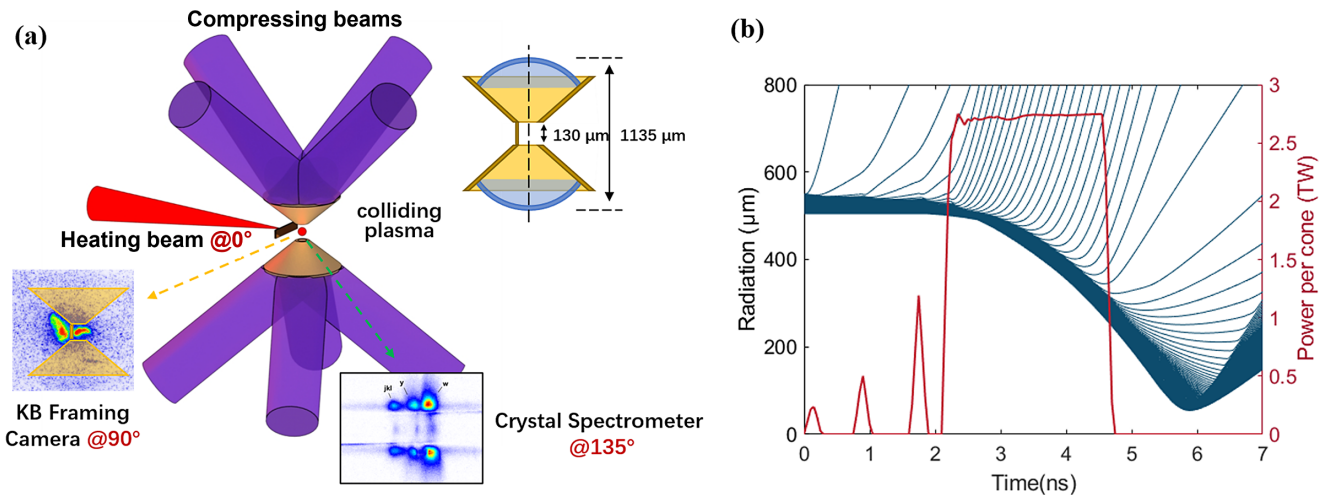


Figure 1. Experimental configuration and laser waveform used in the experiment. (a) Eight driving laser beams are used to directly drive the $CHCl$ shells and push the fuel to collide together at the TCC. The heating laser is injected on a golden plane placed near the TCC to generate fast electrons. (b) The laser waveform and the motion pattern calculated by Multi-1D.

A spatially resolved flat crystal spectrometer was also placed on the equator to diagnose the X-ray spectrum. Its field of view was large enough to observe the colliding and the coronal area. It was set on the rear side of the golden plane at 45° from the normal direction to avoid the interference of the self-emission produced by the heating laser or visual obstruction by the target holder. A potassium acid phthalate (KAP) crystal ($2d = 26.7 \text{ \AA}$) was positioned at 181 cm from the target chamber center (TCC). An SR-type image plate (IP)^[19] was placed 20 cm from the crystal. At the entrance of the spectrometer, a transverse slit of $10 \text{ }\mu\text{m}$ width and 5 mm length was utilized to realize a spatial resolution in the vertical direction. Its spatial resolution is $19.1 \text{ }\mu\text{m}$, which is high enough to distinguish the X-ray from the corona and colliding region. The Bragg angle was set to 9.7° , encompassing a measuring range from 2.66 to 2.85 keV. This range covers the He_α line and the associated satellite lines originating from Cl^{15+} and Cl^{14+} . In order to maintain good contrast, distinct filter configurations were implemented at various heights inside the spectrometer so that faint signals from the colliding area can be detected without any saturation caused by coronal emission. Consequently, the ultimate transmittance was approximately 2% for the corona and 89% for the colliding area.

3. Experimental results

Time-resolved 2D images of the colliding plasmas measured by the KB camera are shown in Figure 2. Figures 2(a)–2(d) show a shot without heating. Figures 2(e)–2(h) show a shot with heating. Figure 2(i) is a schematic geometrical configuration of the Figure 2(f) marked with the targets and the heating laser beam. When the plasmas collide together, the forward kinetic energy is transferred to the internal energy by strong coulomb interaction. The electron temperature increases to 340–390 eV due to the collisional preheating^[18]. The bright spots in Figures 2(a)–2(d) refer to the emission from the colliding plasma. In Figures 2(e)–2(h), the other spots on the left-hand side are caused by the heating

beam. The colliding plasma in Figure 2(b) is approximately $86(\pm 6) \text{ }\mu\text{m}$ high and approximately $120(\pm 6) \text{ }\mu\text{m}$ (normalized intensity above 50%, and the errors come from the KB mirrors and the framing camera together^[18]) without heating. When the heating laser beam is injected at $6.30(\pm 0.08) \text{ ns}$, X-rays caused by the heating beam arise and reach the maximum at $6.46(\pm 0.08) \text{ ns}$. The luminous region caused by the heating laser pulse is shaped by the main cones and the golden plane. As can be seen in Figure 2(i), its central area is aligned with the colliding plasma, indicating good directivity of the heating laser beam. Under the injection of the heating beam, a transverse high-temperature channel (normalized intensity above 50%) is formed with a length of $134 \text{ }\mu\text{m}$ and a height of $53 \text{ }\mu\text{m}$. Compared to the colliding plasma, the self-emission is enhanced by 30% with the heating laser pulse. Meanwhile, the stagnated duration is approximately invariant.

Figure 3(a) shows the space-resolved spectrum from 2.70 to 2.85 keV obtained by the crystal spectrometer. The transverse slit gives the spatial resolution in the vertical direction so that the spectrum can be divided into three regions. The spectrum at the top and the bottom comes from the coronal plasma directly heated by the compressing laser pulses. Between them is the collision area, marked with the red dashed box. The observed spectrum comprises continuous bremsstrahlung emission and line emission of Cl. The line emission consists of a resonance line ('w' at 2789.7 eV, $1s2p \text{ }^1P_1 \rightarrow 1s^2 \text{ }^1S_0$), an intercombination line ('y' at 2775.0 eV, $1s2p \text{ }^3P_1 \rightarrow 1s^2 \text{ }^1S_0$) and a set of Li-like satellite lines ('jkl' and other small peaks)^[20]. Owing to the high energy resolution of $E/\Delta E = 1000$, the spectroscopic analysis reveals three discrete peaks in the coronal and collision regions. As can be seen in Figure 3(b), emission from the colliding region is distinctly enhanced with the injected picosecond heating laser pulse. Since the single cell model that assumes the plasma is uniformly failed to match the experimental result, radiation-hydrodynamic simulations have been implemented to obtain the spatially distributed temperature and density to deduce the temperature by X-ray

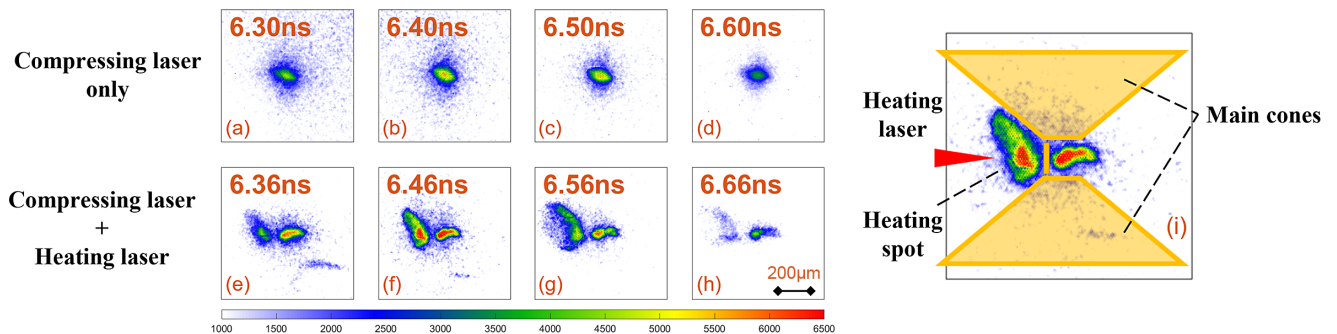


Figure 2. The time-resolved self-emission from the colliding area taken by the KB framing camera. (a)–(d) The X-ray emission of colliding plasmas without the heating laser beam injected. (e)–(h) The heating laser beam is injected from the left-hand side. The spots on the left-hand side are induced by the heating beam. (i) Part of (f) marked with targets and the heating laser beam.

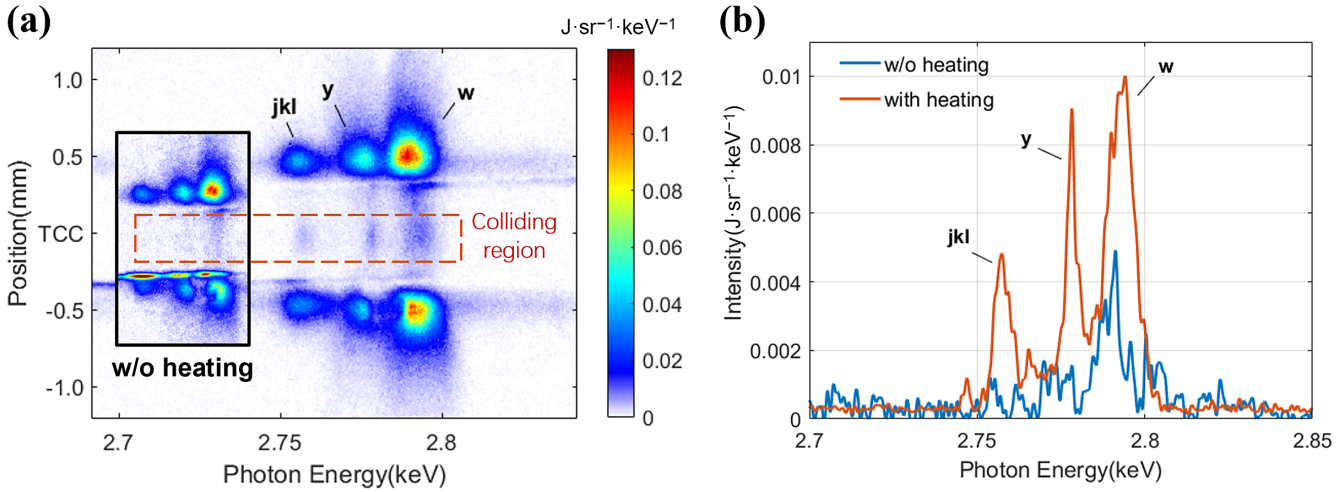


Figure 3. (a) Spatially resolved spectrum of shots with and without (inset) heating. (b) Profiles derived from the TCC position from the two shots (20 μm averaged on and below the TCC position), respectively.

spectroscopy. This will be discussed in the next section. It is worth noting that relative central wavelength shifts are observed between the coronal and collision regions. Specifically, the resonance line (w) exhibited a shift of 4.0 eV, while the intercombination line (y) and the satellite lines (jkl) displayed shifts of 2.5 and 2.0 eV, respectively.

4. Discussion

The enhanced X-ray emission indicates that colliding plasma is heated by the REB generated by the ultra-intense laser pulses. However, simple collision-radiative codes failed to reproduce the measured spectrum. The single cell model assuming a uniform temperature and density distribution is no longer suitable for the colliding plasma. The non-local radiation field becomes important in the calculation due to the high density and the relatively soft X-ray emission. To calculate the spectrum in detail, radiation-hydrodynamics simulation and the scaling theory of fast electrons are used to reproduce the experimental results. Note that the opacity and equation of state tables used in the following simulations are calculated by PROPACEOS code^[21,22].

The processes from compression to head-on collision without the fast heating are simulated by FLASH^[23], an open source radiation-hydrodynamics program. This part is simulated in 2D cylindrical coordinates. Figure 4 shows the simulated results of FLASH at 2.0 and 6.3 ns. In the first 2 ns, the CHCl shell experiences quasi-isentropic compression driven by the three pickets of compressing lasers. Subsequently, the shock wave penetrates the shell, marking the onset of the acceleration phase. Hydrodynamics instabilities grow at the ablation front, leading to density decline. However, with spherical compression and the confinement of the main cone, the density grows to 3 g/cm³ when the fuel is pushed to the apex of the cone. Upon the collision of the two fuel

segments, the forward kinetic energy was efficiently converted into internal energy, primarily facilitated by the strong coulomb collisions. Figures 5(a) and 5(b) show the density and temperature evolution, respectively, of the shell in detail. In Figure 5(c), the transverse distribution of the colliding plasma is presented, as obtained from numerical simulations and experimental density measurements. Experimental density measurements were conducted using monochrome backlight photography combined with Abel inversion^[15]. The simulated results agree well with the experiment in terms of collision time and plasma density distribution.

As for the fast-heating process, the energy deposition of relativistic electrons was evaluated by the following equation^[24,25]:

$$-\frac{dE}{dx} = \frac{2\pi n_e e^4}{m_e \beta^2 c^2} \left(\ln \left(\frac{m_e^2 c^2 (\gamma - 1) \lambda_D^2}{2\hbar^2} \right) + \frac{1}{8} \left(\frac{\gamma - 1}{\gamma} \right)^2 - \frac{2\gamma - 1}{\gamma^2} + 1 - \ln 2 + \ln \left(\frac{u}{\omega_p \lambda_D} \left(\frac{2}{3} \right)^{1/2} \right)^2 \right), \quad (1)$$

where u and n_e are the velocity and the electron density, $\beta = u/c$, $\gamma = (1 - u^2/c^2)^{-1/2}$ is the Lorentz parameter and λ_D and ω_p are the Debye length and the plasma frequency of the colliding plasma, respectively. The considered region is within 600 μm , where the density is above 1×10^{-5} g/cm³ and absorbs the majority of the deposited energy. According to the scaling relation, the temperature of the fast electrons is set to be 1 MeV^[26,27], which is consistent with the experimental results obtained by an IP stack (results to be published). Figure 5(c) shows an example of the temperature distribution before and after fast heating. Note that the heating effects of this calculation mainly provide the profile of the temperature distribution, serving as a reference input for spectral calculations. The final temperature of the stagnated plasma is derived by matching the spectral results.

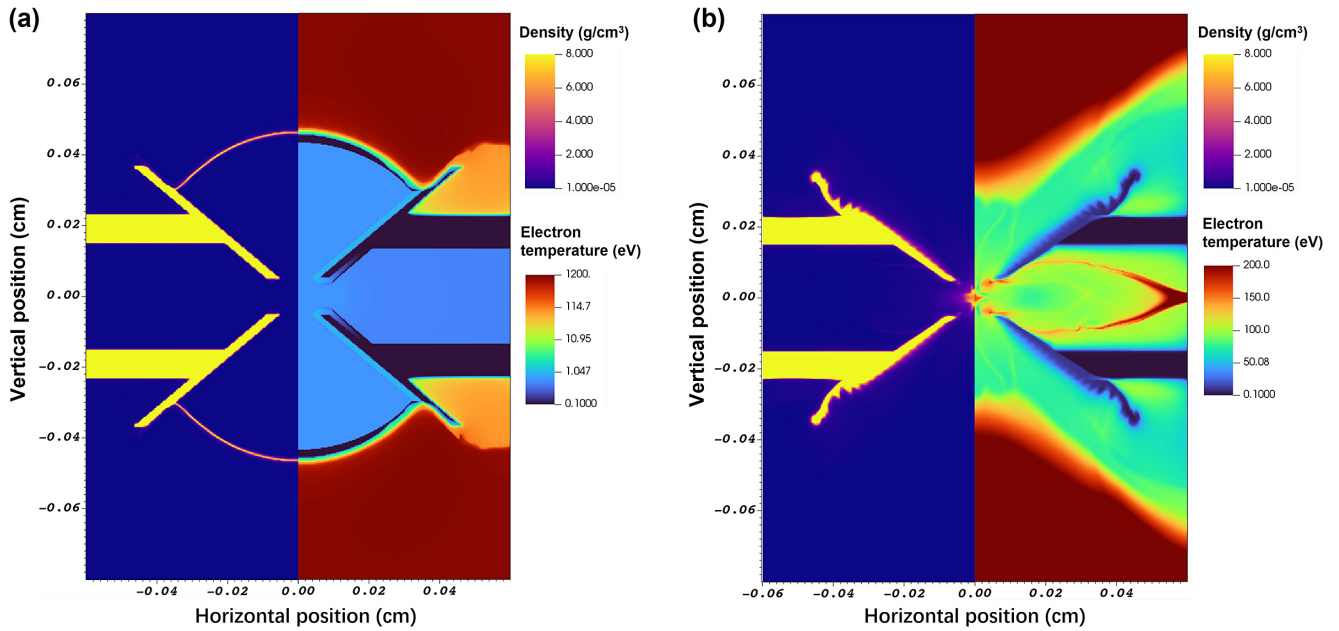


Figure 4. The 2D simulated results of FLASH at (a) 2.0 ns and (b) 6.3 ns. The left-hand side is the density distribution and the right-hand side is the electron temperature distribution. For clarity, the color map of temperature is logarithmic in (a) and linear in (b).

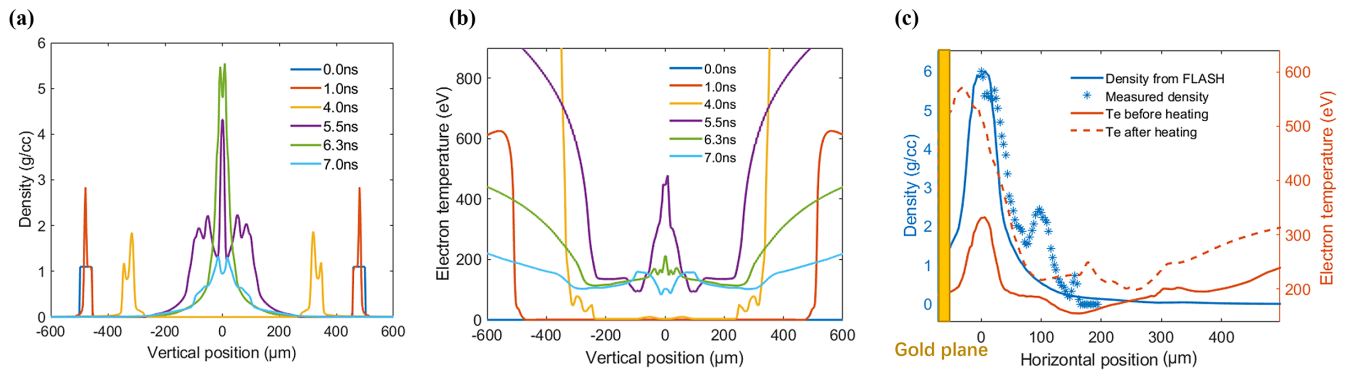


Figure 5. Simulated results used to calculate the spectrum. (a), (b) The density and electron temperature distribution, respectively, in the vertical direction simulated by FLASH. (c) The transverse distribution of the colliding plasma. The simulated density (blue line) is compared with the experimental result (stars). The electron temperature before (red solid line) and after heating (red dotted line) is also shown here.

Plasma spectroscopy has long been used to diagnose plasma parameters^[28–31]. To aid in the qualitative assessment of experiments, plasma models and spectral simulation procedures are often employed. In this context, SPECT3D^[32], a radiation-transport atomic-kinetic code based on a highly detailed atomic model, is used to calculate the K-shell emission from the plasma. Since collisional depopulation affects the population distributions as well as the radiation under such a condition, the collisional-radiative (CR) model is chosen to solve the level populations. Self-consistent coupling with radiation is dealt with by the multi-angle long characteristic model, which computes photon-induced rates by performing radiative transfer along multiple rays that extend through the entire plasma grid. The spectral simulated results are illustrated in Figure 6(a) with experimental data. As the intensities of ‘w’ and ‘jkl’ represent the population

of He-like ions and Li-like ions, respectively, its ratio is commonly used to characterize the plasma temperature when the degree of ionization of the element varies monotonically over the concerned temperature range^[28,30]. Figure 6(b) gives the variation of ionization degree of Cl with temperature for different electron densities. The ratio of population and line intensity varies monotonically in the concerned parameter scale. Hence, it can be concluded that the temperature of the colliding plasma has increased to approximately 600 (±50) eV due to the heating effect induced by fast electrons.

Furthermore, a pronounced blue shift is evident in Figure 6(a). For ‘w’ and ‘y’, two relatively isolated emission peaks, they shift 4.0 and 2.5 eV, respectively. In the case of ‘jkl’, composed of a cluster of satellite lines, the shift of 2.0 eV is determined by analyzing the profile involving the

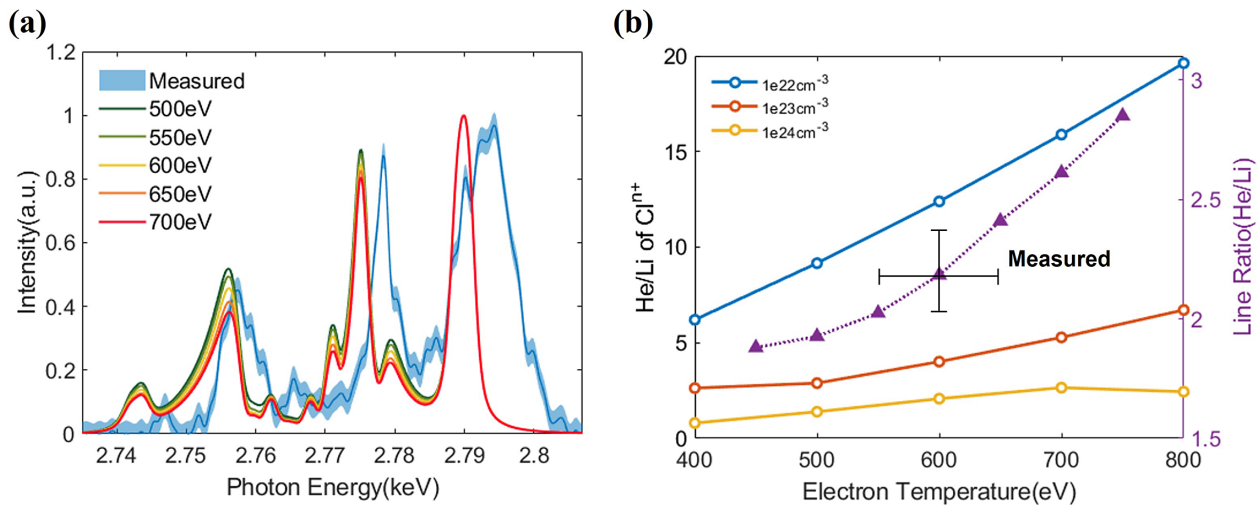


Figure 6. (a) The comparison between the measured and the calculated spectrum. For the calculated results, the temperature range from 500 to 700 eV is included. The measured result is the same as the Figure 3(b) ‘with heating’ with errors marked by the shadow area. The Cl^{n+} population ratio of He-like ions to Li-like ions is shown in (b), together with the line ratio of ‘w’ to ‘jkl’.

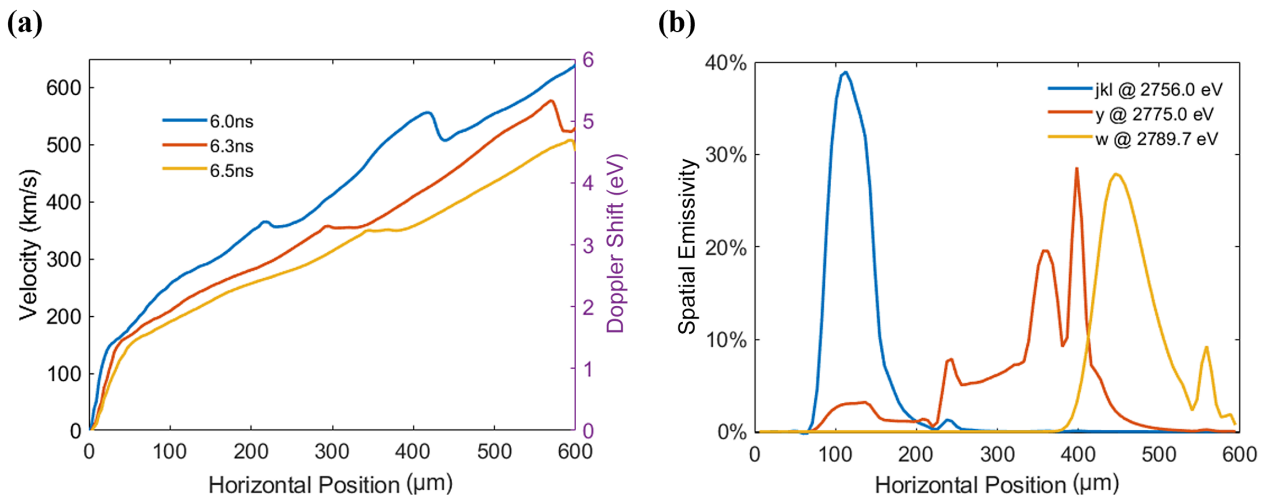


Figure 7. (a) The velocity distribution of the stagnated stage derived from FLASH. (b) Spatial emissivity of the plasma in different depths along the sight line.

rising and falling edges. This phenomenon is the Doppler effect caused by the transverse diffusion of the colliding plasma. The emission peaks emerge from distinct regions of the plasma, each characterized by different diffusion velocities, giving rise to these varying shifts. Figure 7(a) provides insight into the transverse velocity of the plasma, with the right-hand y-axis indicating the Doppler shifts in eV. In Figure 7(b), the spatial emissivity of each emission peak is presented, with each normalized by its own intensity in the spatial position, ensuring that the integral of each line is 100%. This not only explains the energy shift, but also the broadening of the resonance line (‘w’) to a certain extent. According to the spatial emissivity shown in Figure 7(b), the spatial size of line ‘w’ is $450\text{ }\mu\text{m}$ in radius. Its diameter is $900\text{ }\mu\text{m}$, leading to 8.03 eV broadening, accounting for the main part of the broadening compared to the Doppler broadening of 0.88 eV and instrumental broadening of 0.48 eV.

In addition, the spectral results lack temporal resolution, and it is reasonable to infer that the resonance line (‘w’) is emitted over a larger spatial region and for a longer duration, resulting in a significantly greater broadening compared to the intercombination line (‘y’).

5. Conclusions

In summary, an experiment has been conducted at the SG-II UP to investigate the fast heating of an ultra-intense petawatt laser beam in the DCI scheme. After injecting the heating beam, a substantial increase in electron temperature within the high-density stagnated plasma is achieved, leading to the excitation of tracer elements and the emission of K-shell lines. Employing radiation-hydrodynamics simulations and spectral calculations to replicate and diagnose the colliding

plasma, the heated plasma temperature is estimated to be 600 ± 50 eV through the comparison of experimental and simulated results. This notable heating effect is attributed to the favorable alignment between the plasma density and the temperature of the fast electrons. The observed blue shift in the colliding plasma spectrum conveys useful information about its volume velocity and diffusion dynamics, providing additional insights for interpreting the spectral results.

Acknowledgements

The authors would like to thank the DCI joint team for their support of the experiment and the target fabrication. We would like to thank Dr. Yuxue Zhang from the Research Center of Laser Fusion, China Academy of Engineering Physics, and Dr. Feilu Wang from the National Astronomical Observatories, Chinese Academy of Sciences, for their valuable recommendations about analyzing the spectroscopy results.

This work was supported by the Strategic Priority Research Program of the Chinese Academy of Sciences (Grant Nos. XDA25010100, XDA25010300 and XDA25030100) and also in part by the National Natural Science Foundation of China (Grants No. 11827807).

References

1. D. Clery, "With historic explosion, a long sought fusion breakthrough: National Ignition Facility achieves net energy "gain" with laser-powered approach," retrieved from <https://www.science.org/content/article/historic-explosion-long-sought-fusion-breakthrough> (2022).
2. H. Abu-Shawareb, R. Acree, P. Adams, *et al.*, Phys. Rev. Lett. **132**, 065102 (2024).
3. M. Tabak, J. Hammer, M. E. Glinsky, W. L. Kruer, S. C. Wilks, J. Woodworth, E. M. Campbell, M. D. Perry, and R. J. Mason, Phys. Plasmas **1**, 1626 (1994).
4. C. Stoeckl, T. R. Boehly, J. A. Delettrez, S. P. Hatchett, J. A. Frenje, V. Y. Glebov, C. K. Li, J. E. Miller, R. D. Petrasso, F. H. Séguin, V. A. Smalyuk, R. B. Stephens, W. Theobald, B. Yaakobi, and T. C. Sangster, Plasma Phys. Contr. Fusion **47**, B859 (2005).
5. F. Zhang, H. B. Cai, W. M. Zhou, Z. S. Dai, L. Q. Shan, H. Xu, J. B. Chen, F. J. Ge, Q. Tang, W. S. Zhang, L. Wei, D. X. Liu, J. F. Gu, H. B. Du, B. Bi, S. Z. Wu, J. Li, F. Lu, H. Zhang, B. Zhang, M. Q. He, M. H. Yu, Z. H. Yang, W. W. Wang, H. S. Zhang, B. Cui, L. Yang, J. F. Wu, W. Qi, L. H. Cao, Z. Li, H. J. Liu, Y. M. Yang, G. L. Ren, C. Tian, Z. Q. Yuan, W. D. Zheng, L. F. Cao, C. T. Zhou, S. Y. Zou, Y. Q. Gu, K. Du, Y. K. Ding, B. H. Zhang, S. P. Zhu, W. Y. Zhang, and X. T. He, Nat. Phys. **16**, 810 (2020).
6. Y. Kitagawa, Y. Mori, K. Ishii, R. Hanayama, S. Okihara, Y. Arikawa, Y. Abe, E. Miura, T. Ozaki, O. Komeda, H. Suto, Y. Umetani, A. Sunahara, T. Johzaki, H. Sakagami, A. Iwamoto, Y. Sentoku, N. Nakajima, S. Sakata, K. Matsuo, R. S. Mirfayzi, J. Kawanaka, S. Fujioka, K. Tsubakimoto, K. Shigemori, K. Yamanoi, A. Yogo, A. Nakao, M. Asano, H. Shiraga, T. Motohiro, T. Hioki, and H. Azuma, Nucl. Fusion **62**, 096013 (2022).
7. T. Ozaki, Y. Abe, Y. Arikawa, Y. Sentoku, J. Kawanaka, S. Tokita, N. Miyana, T. Jitsuno, Y. Nakata, K. Tsubakimoto, A. Sunahara, T. Johzaki, E. Miura, O. Komeda, A. Iwamoto, H. Sakagami, S. Okihara, K. Ishii, R. Hanayama, Y. Mori, and Y. Kitagawa, Nucl. Fusion **63**, 036009 (2023).
8. P. Norreys, D. Batani, S. Baton, F. N. Beg, R. Kodama, P. M. Nilson, P. Patel, F. Pérez, J. J. Santos, R. H. H. Scott, V. T. Tikhonchuk, M. Wei, and J. Zhang, Nucl. Fusion **54**, 054004 (2014).
9. R. B. Stephens, R. A. Snavely, Y. Aglitskiy, F. Amiranoff, C. Andersen, D. Batani, S. D. Baton, T. Cowan, R. R. Freeman, T. Hall, S. P. Hatchett, J. M. Hill, M. H. Key, J. A. King, J. A. Koch, M. Koenig, A. J. MacKinnon, K. L. Lancaster, E. Martinolli, P. Norreys, E. Perelli-Cippo, M. R. Le Gloahec, C. Rousseaux, J. J. Santos, and F. Scianitti, Phys. Rev. E **69**, 066414 (2004).
10. Z. M. Sheng, Y. Sentoku, K. Mima, J. Zhang, W. Yu, and J. Meyer-ter-Vehn, Phys. Rev. Lett. **85**, 5340 (2000).
11. P. A. Norreys, R. Allott, R. J. Clarke, J. Collier, D. Neely, S. J. Rose, M. Zepf, M. Santala, A. R. Bell, K. Krushelnick, A. E. Dangor, N. C. Woolsey, R. G. Evans, H. Habara, T. Norimatsu, and R. Kodama, Phys. Plasmas **7**, 3721 (2000).
12. R. Kodama, P. A. Norreys, K. Mima, A. E. Dangor, R. G. Evans, H. Fujita, Y. Kitagawa, K. Krushelnick, T. Miyakoshi, N. Miyana, T. Norimatsu, S. J. Rose, T. Shozaki, K. Shigemori, A. Sunahara, M. Tampo, K. A. Tanaka, Y. Toyama, T. Yamanaka, and M. Zepf, Nature **412**, 798 (2001).
13. J. Zhang, W. M. Wang, X. H. Yang, D. Wu, Y. Y. Ma, J. L. Jiao, Z. Zhang, F. Y. Wu, X. H. Yuan, Y. T. Li, and J. Q. Zhu, Philos. Trans. A Math. Phys. Eng. Sci. **378**, 20200015 (2020).
14. W. M. Wang, P. Gibbon, Z. M. Sheng, and Y. T. Li, Phys. Rev. Lett. **114**, 015001 (2015).
15. Z. Zhang, X.-H. Yuan, Y.-H. Zhang, H. Liu, K. Fang, C.-L. Zhang, Z.-D. Liu, X. Zhao, Q.-L. Dong, G.-Y. Liu, Y. Dai, H.-C. Gu, Y.-T. Li, J. Zheng, J.-Y. Zhong, and J. Zhang, Acta Phys. Sin. **71**, 155201 (2022).
16. R. Ramis and J. Meyer-ter-Vehn, Comput. Phys. Commun. **203**, 226 (2016).
17. F. Wu, X. Yang, Y. Ma, Q. Zhang, Z. Zhang, X. Yuan, H. Liu, Z. Liu, J. Zhong, J. Zheng, Y. Li, and J. Zhang, High Power Laser Sci. Eng. **10**, e12 (2022).
18. K. Fang, Y. H. Zhang, Y. F. Dong, T. H. Zhang, Z. Zhang, X. H. Yuan, Y. T. Li, and J. Zhang, Phys. Plasmas **30**, 042705 (2023).
19. Y. Dong, Z. Zhang, M. Xu, Y. Du, C. Zhang, X. Dong, Y. He, J. Tan, Y. Zhang, C. Zhu, J. Feng, L. Cheng, Y. Li, and Y. Li, Rev. Sci. Instrum. **91**, 033105 (2020).
20. A. Kramida, Y. Ralchenko, J. Reader, and NIST ASD Team, "NIST Atomic Spectra Database (version 5.11)," retrieved from <https://physics.nist.gov/asd> (2023).
21. J. J. MacFarlane, I. E. Golovkin, and P. R. Woodruff, J. Quant. Spectrosc. Radiat. Transfer **99**, 381 (2006).
22. C. Orban, M. Fatenejad, and D. Q. Lamb, Phys. Plasmas **29**, 053901 (2022).
23. B. Fryxell, K. Olson, P. Ricker, F. X. Timmes, M. Zingale, D. Q. Lamb, P. MacNeice, R. Rosner, J. W. Truran, and H. Tufo, Astrophys. J. Suppl. Ser. **131**, 273 (2000).
24. C. Deutsch, H. Furukawa, K. Mima, M. Murakami, and K. Nishihara, Phys. Rev. Lett. **77**, 2483 (1996).
25. A. A. Solodov and R. Betti, Phys. Plasmas **15**, 042707 (2008).
26. S. C. Wilks, W. L. Kruer, M. Tabak, and A. B. Langdon, Phys. Rev. Lett. **69**, 1383 (1992).
27. M. G. Haines, M. S. Wei, F. N. Beg, and R. B. Stephens, Phys. Rev. Lett. **102**, 045008 (2009).
28. S. H. Glenzer, C. A. Back, K. G. Estabrook, B. J. MacGowan, D. S. Montgomery, R. K. Kirkwood, J. D. Moody, D. H. Munro, and G. F. Stone, Phys. Rev. E **55**, 927 (1997).

29. M. J. Rosenberg, R. Epstein, A. A. Solodov, W. Seka, J. F. Myatt, P. A. Michel, M. A. Barrios, D. B. Thorn, M. Hohenberger, J. D. Moody, and S. P. Regan, *Phys. Plasmas* **26**, 012703 (2019).
30. L. Gao, B. F. Kraus, K. W. Hill, M. B. Schneider, A. Christopherson, B. Bachmann, M. Bitter, P. Efthimion, N. Pablant, R. Betti, C. Thomas, D. Thorn, A. G. MacPhee, S. Khan, R. Kauffman, D. Liedahl, H. Chen, D. Bradley, J. Kilkenny, B. Lahmann, E. Stambulchik, and Y. Maron, *Phys. Rev. Lett.* **128**, 185002 (2022).
31. B. F. Kraus, L. Gao, W. Fox, K. W. Hill, M. Bitter, P. C. Efthimion, A. Moreau, R. Hollinger, S. Wang, H. Song, and J. J. Rocca, *Phys. Rev. Lett.* **129**, 235001 (2022).
32. J. J. MacFarlane, I. E. Golovkin, P. Wang, P. R. Woodruff, and N. A. Pereyra, *High Energy Density Phys.* **3**, 181 (2007).